

Elastic properties of silicene: Spinodal instabilities

Carlos P. Herrero* and Rafael Ramírez

Instituto de Ciencia de Materiales de Madrid, Consejo Superior de Investigaciones Científicas (CSIC), Campus de Cantoblanco, 28049 Madrid, Spain

(Dated: May 14, 2025)

Silicene, a two-dimensional (2D) allotrope of silicon, has attracted significant interest for its electronic and mechanical properties, alongside its compatibility with various substrates. In this study, we investigate the structural and elastic characteristics of silicene using molecular dynamics simulations based on a tight-binding Hamiltonian, calibrated to align with density-functional theory calculations. We focus particularly on the material's elastic properties and mechanical stability, analyzing its behavior under extensive compressive and tensile in-plane stresses and across temperatures up to 1000 K. Key properties examined include in-plane area, Si-Si bond length, atomic mean-square displacements, elastic constants, and 2D compression modulus. Our findings reveal a notable reduction in stiffness elastic constants, Poisson's ratio, and compression modulus with increasing temperature. Additionally, we identify mechanical instabilities in the silicene structure at specific compressive and tensile biaxial stresses, signaling the material's stability limits or spinodal points. At the corresponding spinodal pressures, structural and elastic properties exhibit anomalies or divergences.

Keywords: Silicene, stress, molecular dynamics, spinodal line

I. INTRODUCTION

Silicene is a two-dimensional allotrope of silicon, which has garnered attention due to its remarkable properties and its potential for diverse applications. Its atomic structure and electronic characteristics offer distinct advantages, positioning it as a promising material for the development of future technologies [1–7].

The significance of silicene lies in its potential role in the semiconductor industry. As a candidate for next-generation electronics, silicene stands out because of its intrinsic semiconducting properties and its seamless compatibility with existing silicon-based technology. With its high electronic mobility and tunable bandgap, it is ideal for high-speed transistors, thereby enhancing the performance of integrated circuits. Beyond electronics, silicene also shows great promise in other fields, as its interaction with light, flexibility, and compatibility with a range of substrates pave the way for applications in photonics, sensing, optoelectronic, and nanoelectromechanical systems [4, 8–15].

Graphene and silicene share a hexagonal lattice structure, yet they exhibit notable differences in their chemical and electronic properties. Graphene is widely celebrated for its exceptional strength and high electronic conductivity, whereas silicene's distinctive buckled structure introduces a bandgap, a feature absent in graphene. This buckling not only influences silicene's electronic properties, but also makes it more chemically reactive, which can impact its stability across various substrates.

For many years, achieving a deep understanding of the thermodynamic properties of two-dimensional (2D) systems has been an objective in statistical physics [16–21]. Traditionally, this topic has been explored within the fields of soft condensed matter and biological membranes [22, 23]. Recently, however, crystalline membranes like

graphene and silicene have emerged as 2D materials that enable the use of realistic interatomic interactions, providing new opportunities to examine the thermodynamic stability of 2D membranes within a three-dimensional (3D) environment. This question has gained renewed interest in recent years, particularly in light of anharmonic couplings between out-of-plane and in-plane vibrations [24–26].

The mechanical properties of silicene, particularly its elastic behavior, have been investigated using a variety of methods. Notably, these include *ab-initio* density-functional-theory (DFT) calculations [27–33], as well as finite-temperature atomistic simulations based primarily on molecular dynamics (MD) [34–39]. This kind of simulations have also been employed to study other properties of silicene: thermal stability and melting behavior [40, 41], thermal conductivity [42], folding and finite-size effects in nanoribbons [43, 44], frictional behavior in multilayer silicene [45], nuclear quantum effects [46], and characteristics of hydrogen-functionalized nanosheets [47]. Experimental and theoretical studies on both monolayers and multilayers of silicene, as well as its potential applications, have been comprehensively reviewed in several publications [3–5, 7, 48, 49].

In this paper, we present and analyze the results of MD simulations of monolayer silicene under varying conditions of external pressure and temperature. Our study examines the effects of in-plane tensile and compressive stress on the structural and elastic properties of this 2D crystalline membrane at temperatures up to 1000 K. The interatomic interactions are modeled using a tight-binding (TB) Hamiltonian fitted to data derived from DFT calculations. We place particular emphasis on silicene's behavior near mechanical instabilities induced by both tensile and compressive stress. These instabilities correspond to spinodal points in silicene's phase diagram,

which mark the stability limits of this 2D membrane.

In this context, the integration of reliable electronic structure calculations with finite-temperature MD simulations offers a powerful framework for examining the interplay among stress, temperature, structure, and electronic properties in 2D materials like silicene. The results of our simulations yield valuable insights into the structural and elastic properties of silicene, providing a basic understanding that could aid in the design and optimization of silicene-based devices.

The paper is organized as follows. In Sec. II, we describe the computational methods used in our study, including the tight-binding approach employed in molecular dynamics simulations. In Sec. III we present the results and discussion as follows: Sec. III.A provides an analysis of the energy of silicene as a function of temperature and applied stress. In Sec. III.B, we present results on the Si–Si bond length, in-plane area, and mean-square displacements of Si atoms. The elastic constants and compression modulus are discussed in Sec. III.C. In Sec. III.D, we examine the spinodal instabilities of silicene under compressive and tensile stress. Finally, the main findings are summarized in Sec. IV.

II. SIMULATION METHOD: TIGHT-BINDING MOLECULAR DYNAMICS

MD simulations are a powerful computational technique for exploring the behavior of materials at the atomic scale. In these simulations, silicon atoms are represented as particles, with their interactions governed by the principles of classical mechanics. The process involves numerically solving Newton’s equations of motion over time, which enables the observation of the dynamic evolution of two-dimensional structures under various conditions. This approach allows for the detailed study of silicene’s response to external factors, such as temperature and applied stress.

We investigate the structural and elastic properties of silicene using MD simulations across a broad range of temperatures and in-plane stresses. A crucial aspect of such simulations is the selection of a reliable method to compute the energy and interatomic forces. The methods available in the literature for this purpose can be categorized into three main groups: (a) empirical interatomic potentials, which employ fitted parameters to reproduce specific material properties [25, 50]; (b) electronic structure methods, such as tight-binding-type Hamiltonians [51, 52]; and (c) *ab initio* techniques, including DFT [53]. Methods of type (a) generally require fewer computational resources, allowing for larger simulation cells and/or extended MD runs. Conversely, methods of type (c) entail significantly higher computational costs for comparable system sizes and simulation times. To balance accuracy and computational efficiency, we adopt an intermediate approach by employing a TB Hamiltonian fitted to DFT calculations. This approach provides a rea-

sonable trade-off between precision and computational feasibility. Note that, although the interatomic forces are derived from a (quantum) electronic-structure method, the dynamics is classical, following Newton’s laws, i.e., nuclear quantum effects are not considered [54–56].

In particular, we calculate the interatomic forces and total energies in silicene using the non-orthogonal TB Hamiltonian presented by Porezag et al. [57], which is based on DFT calculations in the local density approximation (LDA). The TB parameterization for silicon-based materials is detailed in Ref. [58]. In this approach, atomic orbitals are given as eigenfunctions of properly constructed pseudoatoms, having the valence electron charge density concentrated close to the nucleus. The short-range repulsive component of the interatomic potential is calibrated to self-consistent LDA results from selected systems [59]. The overlap and hopping matrix elements have a cutoff of 5.2 Å, encompassing interactions up to third neighbors. It is important to note that the non-orthogonality of the atomic basis ensures the transferability of the TB parameterization to other systems [57]. This TB model has been successfully applied to studies of silicon [52, 58, 60, 61], as well as silicon-containing materials [62–65]. Goringe et al. [59] provided a comprehensive review highlighting the versatility and efficiency of TB methods in accurately describing a wide range of molecular and condensed matter properties.

Our simulations were performed using an in-house code, which has been earlier used for 2D materials as graphene and SiC layers [50, 55, 56, 66]. In particular, the tight-binding formalism employed in our MD method was adapted from the package TROCADERO [67]. In our current implementation of the TB procedure, we sample the electronic degrees of freedom in reciprocal space by considering only the Γ point ($\mathbf{k} = 0$). We have verified that using bigger \mathbf{k} -point sets results in a minor change to the total energy, which has a negligible impact on the energy differences relevant to our study. This change primarily manifests as a slight shift in the minimum energy E_0 , which becomes less significant as the system size increases.

Our MD simulations with the TB Hamiltonian are conducted within the isothermal-isobaric ensemble, where the number of atoms N , the in-plane stress tensor, $\{\sigma_{ij}\}$, and the temperature T are maintained constant. The in-plane stress, measured as a force per unit length, applied at the boundary of the simulation cell, is given in units of eV/Å² or N/m (1 eV/Å² = 16.02 N/m). In the study of 2D materials, such a stress has been also denoted as mechanical or frame tension in the literature [50, 68, 69]. To keep a specified temperature T in our simulations, chains of Nosé-Hoover thermostats were applied to each atomic degree of freedom [70]. Additionally, a separate chain of four thermostats was connected to the barostat that controls the in-plane area of the simulation cell (in the xy plane), ensuring the system maintained the desired stress matrix $\{\sigma_{ij}\}$ [70, 71]. This setup allows for precise control over both temperature and stress during

the simulations, enabling a detailed study of silicene's behavior under various conditions.

The equations of motion were integrated using the so-called reversible reference system propagator algorithm (RESPA), which permits the use of different time steps for fast and slow degrees of freedom within the system [72]. Specifically, we employed a time step of $\Delta t = 1$ fs for the atomic dynamics governed by the TB Hamiltonian, and a smaller time step of $\delta t = 0.25$ fs for the faster dynamical variables, such as those associated with the thermostats. The actual equations of motion employed in our simulations, which were specifically adapted to 2D systems, are given in Ref. [66]. This approach ensures high accuracy in the results obtained for the range of temperatures and stresses considered in this study.

We used rectangular supercells with nearly equal side lengths along the x and y directions in the layer plane, ensuring $L_x \approx L_y$. In most simulations, these supercells contained $N = 112$ silicon atoms, but we also carried out some simulations with 60 and 216 atoms for the sake of comparison. Periodic boundary conditions were applied in the x and y directions, while silicon atoms were allowed to move freely along the out-of-plane z coordinate, where free boundary conditions were implemented. This setup effectively captures the in-plane properties while accommodating any out-of-plane displacements. In the MD simulations, the configuration space was sampled at temperatures T ranging from 50 to 1000 K. For each temperature, a MD run consisted of 2×10^5 steps for equilibration and 5×10^6 steps for computing ensemble averages.

To compare our results for buckled silicene, which represents its equilibrium configuration, we have also carried out MD simulations of planar silicene, assuming a strictly flat hypothetical structure. Several research groups have previously examined this planar configuration using various theoretical methods [3, 4, 42, 73–76]. Comparing data from both planar and buckled silicene provides valuable insights into the energetics and dynamics of this 2D material.

To study the elastic properties of silicene, we applied uniaxial stress in the x or y directions, i.e., $\sigma_{xx} \neq 0$ or $\sigma_{yy} \neq 0$, as well as biaxial stress (2D hydrostatic pressure) P [77], which corresponds to $\sigma_{xx} = \sigma_{yy} = -P$ and $\sigma_{xy} = 0$. It is important to note that $P > 0$ and $P < 0$ represent compressive and tensile stress, respectively, following the conventions of thermodynamics.

The elastic stiffness constants, c_{ij} , of silicene obtained using the TB Hamiltonian in the limit $T \rightarrow 0$ K serve as valuable benchmarks for the finite-temperature values presented below. These elastic constants were calculated from the harmonic dispersion relations of acoustic phonons. To determine the dynamical matrix, we computed the interatomic force constants via numerical differentiation of the energy, based on atomic displacements of 1.5×10^{-3} Å from their minimum-energy positions [46].

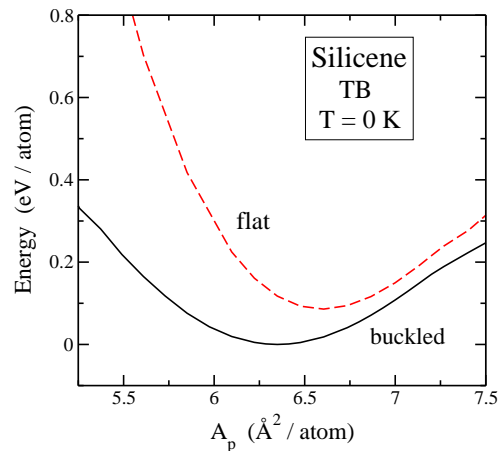


FIG. 1: Energy of silicene as a function of the in-plane area, as obtained with the TB Hamiltonian used in this paper. The solid line corresponds to the buckled configuration, while the dashed curve indicates the energy of flat silicene. The zero of energy is taken for the minimum-energy (buckled) configuration at $A_p^0 = 6.351$ Å²/atom.

III. RESULTS AND DISCUSSION

A. Energy

In this section, we study the dependence of silicene's energy on temperature and applied stress, as derived from our MD simulations. In Fig. 1, we display the energy at $T = 0$ K, as a function of the in-plane area A_p , obtained with the TB Hamiltonian employed here. The solid curve indicates the result for the buckled configuration, whereas the dashed line corresponds to the energy of flat silicene. For a given A_p , silicon atoms are relaxed to the state with minimum energy compatible with this area, leaving them free on the three space directions for buckled silicene, and restricted to stay on the $z = 0$ plane for the flat configuration. The absolute minimum is found for buckled silicene with an in-plane area $A_p^0 = 6.351$ Å²/atom, and its energy, E_0 , is taken as the reference for the values shown in Fig. 1. For planar (strictly flat) silicene, we found a minimum energy of 86 meV/atom above the absolute minimum E_0 , corresponding to an area $A_p = 6.595$ Å²/atom. This energy difference means an appreciable energy barrier which favors the buckled structure. As shown in Fig. 1, the energy difference between both configurations, planar and buckled, increases fast as the in-plane area is reduced, and for $A_p = 5.6$ Å²/atom it amounts to 0.54 eV/atom.

Turning to the effect of pressure, in Fig. 2, we present the energy $E - E_0$ of silicene as a function of applied biaxial stress for three temperatures: $T = 100$ K (circles), 500 K (squares), and 1000 K (diamonds). For comparison, the solid line represents the pressure dependence for $T = 0$ K. We find that the energy increases as one departs from the stress-free conditions in all cases shown in

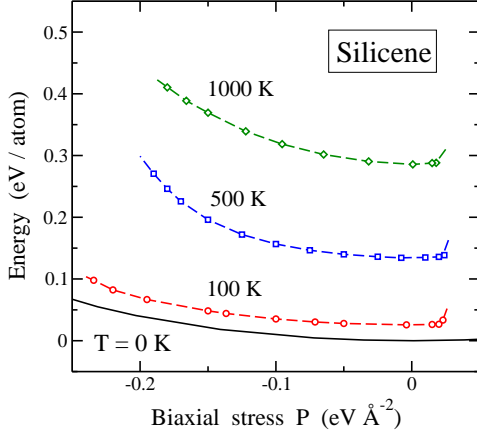


FIG. 2: Energy of silicene as a function of biaxial stress. Symbols indicate results of MD simulations at three temperatures: $T = 100$ K (circles), 500 K (squares), and 1000 K (diamonds). The solid line is the result for $T = 0$ K.

Fig. 2, for both tension $P < 0$ and compression $P > 0$. For $P = 0$, the simulation data at different temperatures closely follow the harmonic expression $E = E_0 + 3k_B T$ (k_B , Boltzmann's constant), but they slowly tend to become higher than the harmonic expectancy as temperature increases, due to anharmonicity of the interatomic potential. For stressed silicene, we observe that the energy change for different temperatures is not constant when stress is varied, especially for $P < 0$. The departure of the energy from the harmonic expectation is only due to the potential energy, since the kinetic energy per atom in a classical model remains constant, $E_{\text{kin}} = 3k_B T/2$, irrespective of anharmonicity. The energies $E - E_0$ discussed here were found to be insensitive to the system size, i.e., results obtained for $N = 112$ and 216 atoms coincide within the statistical error bar of the simulation method.

Eventually, the 2D material becomes unstable for particular values of both tensile and compressive stress, which depend on the temperature. These stress values delineate the stability region for silicene at each temperature, and lie around a tensile stress of $-0.2 \text{ eV } \text{\AA}^{-2}$ and a compressive one of $25(1) \text{ meV } \text{\AA}^{-2}$. This will be discussed in more detail below.

We note that a classical description, as that presented here, will lose precision at low temperatures, due to the onset of nuclear quantum motion and its associated zero-point energy [46, 55]. This will, however, not be relevant for the effects considered here.

B. Silicene structure

1. Si-Si bond length

For the minimum-energy configuration of silicene, the TB Hamiltonian predicts a buckled chair-like structure, with an interatomic distance $d_{\text{Si-Si}}^0 = 2.284 \text{ \AA}$, to be compared with data derived from several DFT calculations, which range from 2.24 to 2.28 \AA [73–75, 78]. For the Si-Si-Si angle, we find $\phi = 113.90^\circ$, intermediate between a strictly flat silicene, with $\phi = 120^\circ$ (sp^2 electronic hybridization in Si atoms) and $\phi = 109.47^\circ$ for sp^3 hybridization in bulk silicon (tetrahedral coordination). The difference in z coordinate between nearest neighbors obtained with the TB model amounts to $h = 0.574 \text{ \AA}$ (buckling distance). For planar silicene ($h = 0$), we found an interatomic distance of 2.253 \AA , a little shorter than for the buckled structure.

From our simulations at finite temperatures, we obtain a dependence for the distance $d_{\text{Si-Si}}$ which can be well described up to $T = 1000 \text{ K}$ by a quadratic expression: $d_{\text{Si-Si}} = d_{\text{Si-Si}}^0 + a_1 T + a_2 T^2$, with $a_1 = 1.91 \times 10^{-5} \text{ \AA/K}$ and $a_2 = 3.26 \times 10^{-8} \text{ \AA/K}^2$. This quadratic function indicates an appreciable departure of linearity in the temperature dependence of the interatomic distance [46]. Such nonlinearity is more appreciable when compared with other two-dimensional crystalline solids as graphene [55] or SiC monolayers [56], mainly attributed to the silicene buckled structure, which enhances bond expansion for increasing T . Additional information about this nonlinearity can be obtained from comparison with results of simulations for planar silicene, which yield a temperature dependence of $d_{\text{Si-Si}}$ approximately linear in a temperature range broader than for buckled silicene.

The buckling distance h derived from our MD simulations decreases slightly for rising T , and at 800 K we find $h = 0.561 \text{ \AA}$. Note that h is an average value of the difference in z coordinates of silicon atoms, calculated along a simulation run. The actual difference fluctuates within each atomic configuration, as well as the mean value along successive simulation steps, and such fluctuations appreciably increase for rising T . At 300 K , h decreases from 0.565 \AA for stress-free silicene to 0.508 \AA for tensile stress $P = -0.17 \text{ eV } \text{\AA}^{-2}$, and then it increases under larger tension, due to the larger fluctuations in the z coordinate close to the spinodal instability P_c (see below). For $P = -0.22 \text{ eV } \text{\AA}^{-2}$ we find $h = 0.603 \text{ \AA}$.

In Fig. 3 we present the interatomic distance between nearest neighbors as a function of biaxial stress for three temperatures: $T = 300 \text{ K}$ (circles), 500 K (squares), and 1000 K (diamonds). We also display the $T = 0 \text{ K}$ result, shown as a solid line. In the zero-temperature limit ($T \rightarrow 0 \text{ K}$), we find an increase in $d_{\text{Si-Si}}$ for rising tension, which at $P = 0$ is given by $\partial d_{\text{Si-Si}} / \partial P = -0.16 \text{ \AA}^3/\text{eV}$. The slope of the decreasing curve grows under tensile stress, and eventually diverges to $-\infty$ for $P = -0.32 \text{ eV } \text{\AA}^{-2}$, where the system becomes unstable at $T = 0 \text{ K}$. The slope at $P = 0$ increases for rising temperature, and

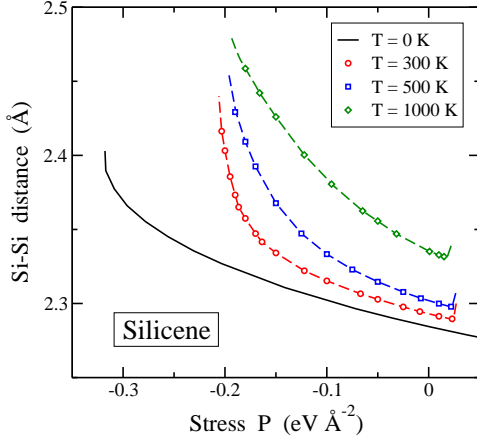


FIG. 3: Pressure dependence of the mean Si-Si distance, $d_{\text{Si-Si}}$. Open symbols represent results of MD simulations at various temperatures: $T = 300$ K (circles), 500 K (squares), and 1000 K (diamonds). The solid line indicates the interatomic distance at $T = 0$ K.

at $T = 1000$ K we find $\partial d_{\text{Si-Si}}/\partial P = -0.32 \text{ Å}^3/\text{eV}$.

For finite temperatures in general, we observe that the distance $d_{\text{Si-Si}}$ grows faster for rising tensile stress, and reaches values larger than 2.4 Å for $P \approx -0.2 \text{ eV Å}^{-2}$, near the limit of mechanical stability for the temperatures shown in Fig. 3. For compressive stress, we do not observe any clear anomaly when approaching the stability limit, until the collapse of the silicene structure into a corrugated configuration.

2. Area of the silicene layer

In this section, we analyze the behavior of A_p as a function of both temperature and biaxial stress, considering tensile and compressive regimes. The isothermal-isobaric ensemble employed here treats the in-plane area $A_p = L_x L_y / N$ as the variable conjugate to the applied stress P . The temperature dependence of A_p has previously been explored for silicene through MD simulations for external stress $P = 0$. For the buckled minimum-energy configuration, we find the in-plane area $A_p^0 = 6.351 \text{ Å}^2/\text{atom}$, which aligns with earlier calculations [46], and corresponds to a lattice parameter of the hexagonal unit cell: $a_0 = 3.830 \text{ Å}$. The area A_p is related to the projection d_{xy} of Si-Si bonds on the xy plane as $A_p = 3\sqrt{3}d_{xy}^2/4$, with $d_{xy}^2 = d_{\text{Si-Si}}^2 - h^2$. These expressions are precise at low T , but they become less accurate for increasing temperature, due to the larger atomic motion and the associated bending of the silicene layer.

For stress-free silicene, where $P = 0$, the in-plane area A_p decreases as the temperature rises from $T = 0$ K to approximately 450 K, i.e., $\partial A_p/\partial T < 0$. A minimum of A_p is observed at this temperature ($T_m \approx 450$ K). The dependence of A_p on T is governed by two pri-

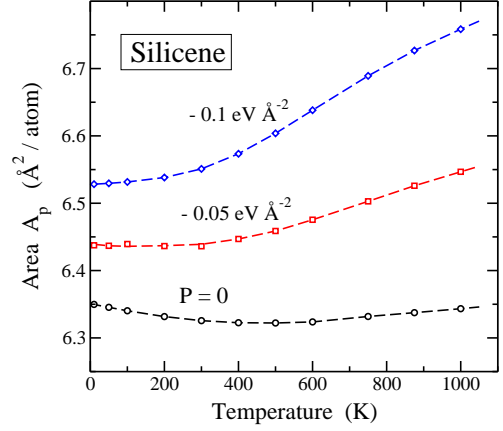


FIG. 4: Temperature dependence of the in-plane area A_p . Symbols indicate results of MD simulations for $P = 0$ (circles), -0.05 eV Å^{-2} (squares), and -0.1 eV Å^{-2} . Dashed lines are guides to the eye. Error bars are in the order of the symbol size.

mary factors: atomic out-of-plane motion, which tends to reduce A_p , and thermal expansion of the interatomic bonds, which drives an increase in the in-plane area. At low temperatures, the first factor predominates, whereas above $T \approx 450$ K, the second factor becomes more significant [46].

It is noteworthy that the in-plane area A_p for planar silicene at $T = 0$ K is $6.595 \text{ Å}^2/\text{atom}$, which is larger than that of the buckled configuration. In the planar structure, thermal expansion is observed as T increases, without the initial decrease in A_p seen in buckled silicene at low temperatures.

Fig. 4 illustrates the temperature dependence of the in-plane area A_p of buckled silicene for $P = 0$, -0.05 , and -0.1 eV Å^{-2} . The key observation is that the decrease in A_p seen in the stress-free material at temperatures below T_m vanishes under tensile stress. For $P = -0.05 \text{ eV Å}^{-2}$, the derivative $\partial A_p/\partial T$ is close to zero at low temperatures, while for higher tensile stress, such as $P = -0.1 \text{ eV Å}^{-2}$, this derivative becomes positive, as shown in the figure. This behavior can be attributed to a reduction in the amplitude of out-of-plane vibrations (in the z direction) under tensile stress ($P < 0$), as discussed further in Sec. III.B. These atomic vibrations have less influence on the thermal behavior of A_p in the presence of tensile stress.

In Fig. 5 we display the dependence of the in-plane area A_p on biaxial stress P at three temperatures: $T = 300$ K (circles), 500 K (squares), and 1000 K (diamonds). The solid line represents the result for $T = 0$ K. Stress-induced changes in A_p are related to linear strain ϵ_L by the expression: $A_p = A_p^0(1 + \epsilon_L)^2$. Then, the area range in the vertical axis of Fig. 5 corresponds to a strain region between $\epsilon_L = -6.9 \times 10^{-2}$ (compression) and 0.12 (tension).

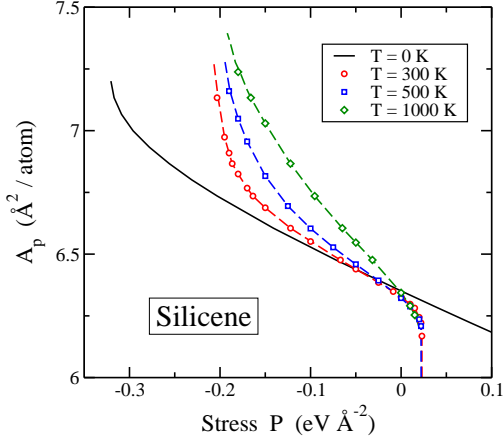


FIG. 5: In-plane area as a function of biaxial stress P , for three temperatures: $T = 300$ K (circles), 500 K (squares), and 1000 K (diamonds). The solid line corresponds to $T = 0$ K. Dashed lines are guides to the eye.

At $T = 0$ K, we identify the stability limit of silicene under tensile stress at $P_c = -0.32$ eV \AA^{-2} , which coincides with the limit found for the Si-Si bond length in Sec. III.B. At finite temperatures, this threshold shifts to approximately -0.2 eV \AA^{-2} , in line with results for the Si-Si distance shown above in Fig. 3. Under compressive stress, silicene remains stable at $T = 0$ K up to large stress values, without any discontinuity in the in-plane area or in the other variables considered here. At finite temperatures, the spinodal pressure emerges for $P'_c = 24(1)$ meV \AA^{-2} , with the temperature effect being smaller than the statistical error margin. Note that the larger stability limit of the silicene layer at $T = 0$ K compared to the finite-temperature results is due to the absence of out-of-plane motion, which causes the breakdown of the structure for $T > 0$ K.

At the spinodal pressure P'_c , the derivative $\partial A_p / \partial P$ diverges to $-\infty$, which is an indication of the vanishing of the compression modulus B_p (see below). B_p also vanishes for tensile biaxial stress $P_c < 0$, but in this case the divergence in the stress derivative of A_p is not so clearly observable, as the simulated 2D layer becomes unstable in the region close to P_c , with large A_p fluctuations.

3. Mean-square displacements of Si atoms

In this section we study the mean-square displacement (MSD) of silicon atoms in the xy layer plane, as well as in the out-of-plane z direction. This gives us information on the overall changes of vibrational amplitudes as temperature and/or external stress are modified, and their influence on the mechanical stability of the silicene layer. For a given atomic coordinate (say z), we define the MSD as $(\Delta z)^2 = \langle (z - \bar{z})^2 \rangle$, where the angle brackets indicate the mean value along a MD trajectory, and $\bar{z} = \langle z \rangle$ is the

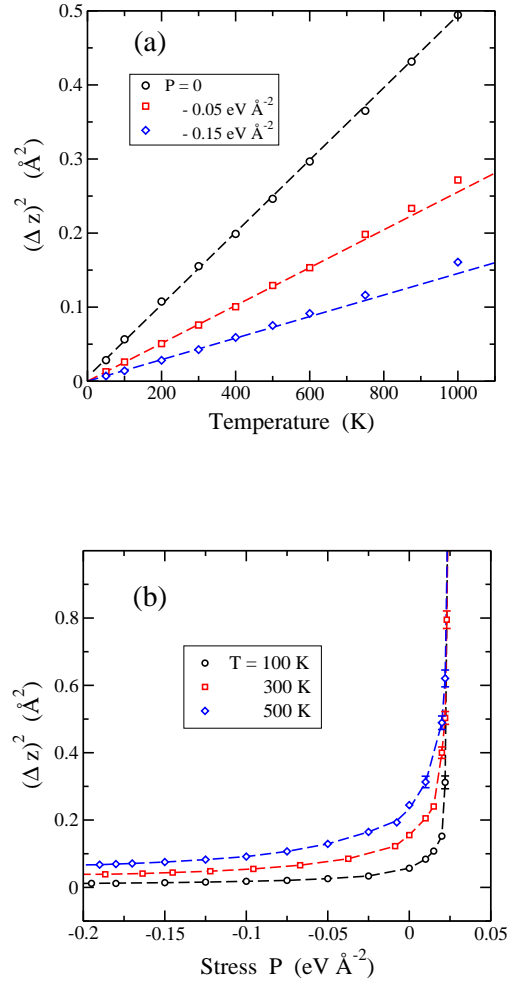


FIG. 6: Atomic MSD, $(\Delta z)^2$, along the out-of-plane direction. (a) Temperature dependence for biaxial stress $P = 0$ (circles), -0.05 eV \AA^{-2} (squares), and -0.15 eV \AA^{-2} (diamonds). Dashed lines are linear fits to the data points for $T < 600$ K. (b) Stress dependence at three temperatures: $T = 100$ K (circles), 300 K (squares), and 500 K (diamonds). Lines are guides to the eye. Error bars in (a) and (b), when not displayed, are of the order of the symbol size.

average value of the considered coordinate.

In Fig. 6(a) we display the temperature dependence of the out-of-plane MSD, $(\Delta z)^2$. Symbols indicate results of MD simulations for $P = 0$ (circles), -0.05 eV \AA^{-2} (squares), and -0.15 eV \AA^{-2} (diamonds). The obtained dependence of $(\Delta z)^2$ on T is rather linear, mainly at low temperature, and deviations from linearity are observed at high T , mainly in the presence of tensile stress. The slope of the lines shown in Fig. 6(a) decreases for increasing tensile stress. Thus, from linear fittings of the data points for $T < 600$ K we find $\partial(\Delta z)^2 / \partial T = 4.8 \times 10^{-4}$, 2.6×10^{-4} , and 1.5×10^{-4} $\text{\AA}^2/\text{K}$ for $P = 0$, -0.05 , and -0.15 eV \AA^{-2} , respectively. Note that the latter is less than a third of the value corresponding to the unstressed material.

In Fig. 6(b) we show the mean-square displacement

$(\Delta z)^2$ for $N = 112$ as a function of applied biaxial stress P , derived from MD simulations for $T = 100$ K (circles), 300 K (squares), and 500 K (diamonds). Looking at the $P < 0$ region, we observe a smooth decrease of the MSD for rising tensile stress. This decrease is more important for P in the region from 0 to -0.1 eV \AA^{-2} , and for larger stresses, the reduction of $(\Delta z)^2$ is slower. The vibrational amplitudes decrease for increasing tensile stress, as a consequence of the rise in frequency of the transverse modes. This is more appreciable for higher T , but it is also observed in the low-temperature region, as shown for $T = 100$ K. The most striking feature in Fig. 6(b) is the fast rise of the out-of-plane MSD observed for compressive stress ($P > 0$). This happens similarly for the different temperatures considered in our simulations, and indicates a divergence for all of them at $P'_c \approx 24$ meV \AA^{-2} . This is consistent with the appearance of an instability for silicene under this compressive stress.

As indicated above, the configuration of silicene for $T \rightarrow 0$ K corresponds to a buckled structure. The vertical displacement between nearest-neighbor Si atoms, or buckling distance, is $h = 0.57$ \AA [46]. At finite temperatures, the silicene layer bends due to atomic motion in the z direction. In a classical harmonic approximation, the contribution to the MSD of a vibrational mode with frequency ω is proportional to $1/\omega^2$, so that the largest contribution comes from low-frequency modes. For the out-of-plane direction, these are ZA modes with wavevector close to $\mathbf{k} = 0$ (Γ point), i. e., small wavenumber $k = |\mathbf{k}|$.

For stress-free silicene, the ZA phonon branch can be described close to the Γ point by a dispersion relation of the form

$$\rho\omega(\mathbf{k})^2 = \gamma_0 k^2 + \kappa k^4. \quad (1)$$

From an analysis of the bands obtained with the TB Hamiltonian employed here [46], we find a bending constant $\kappa = 0.39(2)$ eV. For small k , the frequency increases linearly with k , i.e., $\omega(\mathbf{k}) \approx \sqrt{\gamma_0/\rho} k$ for $k \ll 1$ \AA^{-1} . External stress affects the mode frequencies in the crystalline membrane, causing changes in the vibrational amplitudes. Thus, under a biaxial stress P , the first term on the r.h.s. of Eq. (1) is replaced by γk^2 , with $\gamma = \gamma_0 - P$. This means that the importance of this term is enhanced for $P < 0$ (tensile stress) and reduced for $P > 0$ (compressive stress).

One expects a mechanical instability of the silicene structure when the compressive stress P approaches γ_0 , i.e., for $\gamma \rightarrow 0$. For larger stresses, one has $\gamma < 0$, with the appearance of unphysical imaginary frequencies close to the Γ point. The critical pressure P'_c is expected to depend on the system size N , and is connected with the fluctuations of the in-plane area A_p , which also diverge in parallel with $(\Delta z)^2$. This is discussed in Sec. III.C in relation with the 2D modulus of compression B_p , which vanishes at P'_c .

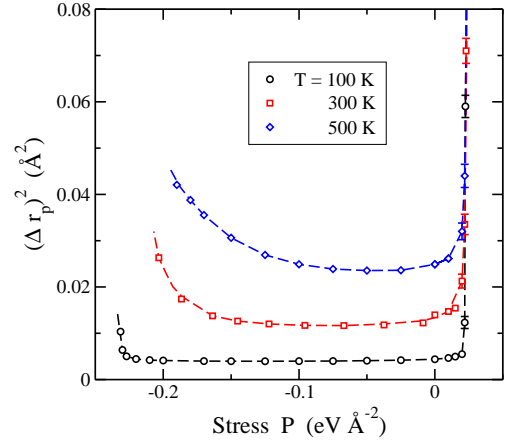


FIG. 7: MSD $(\Delta \mathbf{r}_p)^2$ of Si atoms in the xy plane as a function of biaxial stress P . Open symbols are data points obtained from MD simulations at three temperatures: $T = 100$ K (circles), 300 K (squares), and 500 K (diamonds). Lines are guides to the eye. Error bars, when not shown, are in the order of the symbol size.

In Fig. 7 we present the in-plane mean-square displacement, $(\Delta \mathbf{r}_p)^2 = (\Delta x)^2 + (\Delta y)^2$, as a function of biaxial stress for $T = 100$ K (circles), 300 K (squares), and 500 K (diamonds). We observe a fast increase in the MSD under compressive stress, with a divergence at $P'_c \approx 24$ meV \AA^{-2} for the three temperatures. Moreover, in contrast to the results for $(\Delta z)^2$, we find an increase in $(\Delta \mathbf{r}_p)^2$ under tensile stress. For low temperature ($T = 100$ K), the structure becomes unstable for $P_c = -0.23$ eV \AA^{-2} . At higher T , we find the instability at $P_c \approx -0.20$ eV \AA^{-2} .

The reason for the different behavior of the MSD of Si atoms on the in-plane and out-of-plane directions for $P < 0$ is related to the weakening of Si-Si bonds when the interatomic distance increases under tension. This is in line with the behavior of the in-plane area A_p for $P < 0$, displayed in Fig. 5. Even though the Si-Si bonds are not strictly parallel to the layer plane, as indicated by a buckling distance $h = 0.47$ \AA at low T , the effect of their weakening on the out-of-plane atomic displacements is small enough to not be observed under tensile stress.

C. Elastic constants and compressibility

MD simulations provide a valuable tool for investigating the elastic properties of materials subjected to various types of applied stresses, such as uniaxial or biaxial stress. In this study, we focus on determining the elastic stiffness constants, c_{ij} , and compliance constants, s_{ij} , for silicene crystalline layers, which possess a hexagonal 2D structure. We denote the components of the strain and stress tensors as e_{ij} and σ_{ij} , respectively. The strain components follow the conventional notation: $e_{ij} = \epsilon_{ij}$

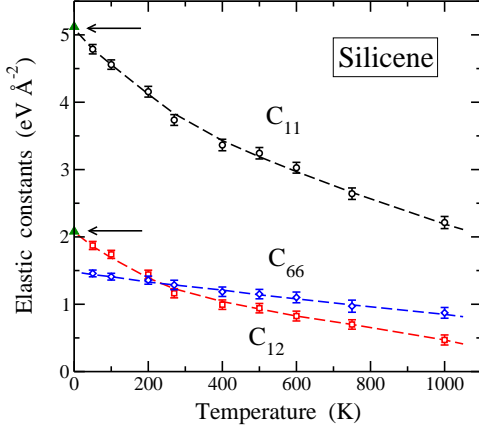


FIG. 8: Elastic constants of silicene as a function of temperature. Symbols are data points derived from MD simulations for c_{11} (circles), c_{12} (squares), and c_{66} (diamonds). Triangles at $T = 0$ K indicate values of c_{11} and c_{12} derived from the LA and TA phonon bands, and are signaled by arrows. Error bars of the simulation data, when not shown, are on the order of the symbol size. Lines are guides to the eye.

when $i = j$, and $e_{ij} = 2\epsilon_{ij}$ when $i \neq j$ [79, 80].

For a general applied stress $\{\sigma_{ij}\}$, the strain components are given through the compliance constants as:

$$\begin{pmatrix} e_{xx} \\ e_{yy} \\ e_{xy} \end{pmatrix} = \begin{pmatrix} s_{11} & s_{12} & 0 \\ s_{12} & s_{11} & 0 \\ 0 & 0 & 2(s_{11} - s_{12}) \end{pmatrix} \begin{pmatrix} \sigma_{xx} \\ \sigma_{yy} \\ \sigma_{xy} \end{pmatrix}. \quad (2)$$

The stiffness constant matrix, $\{c_{ij}\}$, is the inverse of the compliance matrix, $\{s_{ij}\}$. These matrices are related by the expressions $c_{11} = s_{11}/Z$, and $c_{12} = -s_{12}/Z$, where $Z = s_{11}^2 - s_{12}^2$. For a more detailed discussion of the elastic properties of 2D materials, see Ref. [77].

The compliance constants were obtained by applying small uniaxial stresses, σ_{xx} or σ_{yy} , in MD simulations conducted at various temperatures, using Eq. (2). From the computed s_{ij} values, the corresponding stiffness constants c_{ij} were then derived. The temperature dependence of c_{ij} is shown in Fig. 8, where a notable decrease in c_{11} and c_{12} is observed as temperature increases. Specifically, at $T = 1000$ K, these elastic constants are reduced by 57% and 77%, respectively, compared to their values at $T = 0$ K. Additionally, values of c_{66} in Fig. 8 were calculated as $c_{66} = (c_{11} - c_{12})/2$. In this case, the reduction from $T = 0$ K to 300 and 1000 K amounts to 16% and 43% of the low-temperature value, respectively. In Fig. 8, solid triangles at $T = 0$ K, indicated by arrows, display results for c_{11} and c_{12} derived from the slope of the phonon dispersion bands close to the Γ point (harmonic approximation). Outcomes of finite-temperature MD simulations for the stiffness constants converge at low T to the results of the harmonic approximation for both c_{11} and c_{12} . The decrease in these elastic constants for increasing temperature is a consequence of the intrinsic anharmonicity of the interatomic potential, which

causes an elongation of the Si-Si bonds with rising T (see Fig. 3). The weakening of the interatomic bonds implies that the vibrational modes of the layer shift to lower frequencies. This is reflected in a reduction of the compression modulus of the layer, B_p , as the temperature increases (see below).

The Poisson's ratio, ν , which quantifies the deformation in a direction perpendicular to an applied stress, can be determined from the elastic constants using the relation $\nu = c_{12}/c_{11}$. For $T \rightarrow 0$, we find for silicene $\nu = 0.41$. At finite temperatures, our MD simulations show a decrease in ν . Specifically, for $T = 300$ and 1000 K, the values of ν drop to 0.30 and 0.21, respectively. Results of first-principles calculations given in the literature for the Poisson's ratio of monolayer silicene are in the range from 0.31 to 0.41 [28, 32, 33, 81].

For layered materials, the 2D modulus of hydrostatic compression, B_p , at a given temperature T , is defined as $B_p = -A_p(\partial P/\partial A_p)_T$. Here, the biaxial pressure P , in the isothermal-isobaric ensemble used in our simulations, is the conjugate variable to the in-plane area A_p . Alternatively, the modulus B_p can be calculated using the fluctuation formula [50, 82, 83]:

$$B_p = \frac{k_B T A_p}{N(\Delta A_p)^2}, \quad (3)$$

where $(\Delta A_p)^2$ represents the mean-square fluctuation of the area A_p . This fluctuation-based expression enables us to compute B_p from MD simulations at $P = 0$ without the need to perform numerical derivatives over data for different applied pressures. We have verified, for selected temperatures, that the B_p values obtained using both methods (A_p fluctuations and numerical derivative) agree within the simulation error bars.

For 2D materials with hexagonal symmetry, such as silicene, the modulus B_p can be also derived from the elastic constants using the relation $B_p = (c_{11} + c_{12})/2$. The temperature dependence of B_p , as obtained from our simulations, is shown in Fig. 9. This figure presents data derived from two methods: stiffness constants (solid circles) and the fluctuation formula in Eq. (3) (open circles). Both sets of results are in good agreement, within the precision indicated by their respective statistical error bars. For $T \rightarrow 0$ K, the modulus B_p^0 can be determined from the second derivative of the energy (shown in Fig. 1) with respect to the area A_p , $B_p^0 = A_p^0(\partial^2 E/\partial A_p^2)_0$, yielding $B_p^0 = 3.73$ eV \AA^{-2} . This value, marked in Fig. 9 by a horizontal arrow, aligns with the extrapolation of finite-temperature data to $T = 0$ K.

The 2D Young's modulus, E_p , can be calculated from the compression modulus B_p and the Poisson's ratio ν using the relation $E_p = 2B_p(1 - \nu)$. For silicene, this yields from our calculations $E_p = 4.40$ eV \AA^{-2} at $T = 0$ K and 3.37 eV \AA^{-2} at 300 K. For comparison, values reported for B_p from DFT calculations (average of armchair and zigzag directions) lie between 3.56 and 3.86 eV \AA^{-2} [28, 32, 33].

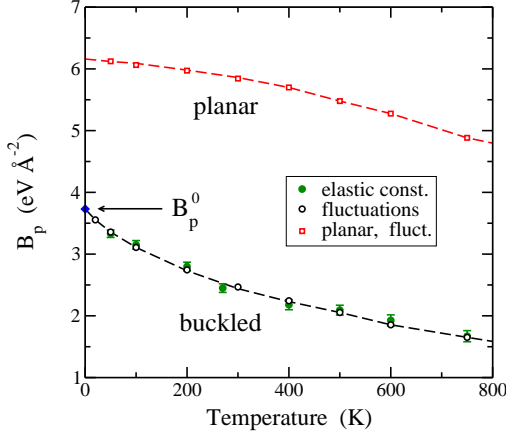


FIG. 9: Temperature dependence of the compression modulus B_p of silicene. Circles represent results for buckled silicene obtained from the area fluctuations (open circles, Eq. (3)), and from the elastic constants c_{11} and c_{12} (solid circles). Open squares correspond to the modulus B_p of planar silicene, derived from the area fluctuations at several temperatures. Error bars, when not shown, are on the order of the symbol size. Lines are guides to the eye.

For comparison with our results for buckled silicene, Fig. 9 also displays the temperature dependence of the modulus B_p for planar (strictly flat) silicene, derived from similar MD simulations. As expected, the flat structure exhibits a significantly higher B_p , consistent with its increased rigidity. In the limit $T \rightarrow 0$ K, B_p^0 for planar silicene is found to be $6.16 \text{ eV } \text{\AA}^{-2}$.

D. Spinodal instabilities

In the preceding sections, we have shown the emergence of instabilities in the silicene structure when subjected to specific in-plane stresses, whether compressive or tensile. These instabilities manifest through the behavior of various physical variables, as illustrated in multiple plots: energy (Fig. 2), Si-Si bond length (Fig. 3), in-plane area A_p (Fig. 5), and atomic MSD for both out-of-plane motion (Fig. 6(b)) and in-plane motion (Fig. 7). In several instances, though not universally, these instabilities are evident as a divergence in the examined variable or its pressure derivative. This divergence is particularly pronounced in the atomic MSD and the in-plane area A_p .

From a thermodynamic perspective, mechanical instabilities in solids are typically characterized by a divergence in compressibility or the vanishing of its inverse, the bulk modulus, in 3D materials. A similar behavior is expected in 2D crystalline membranes like silicene, where the compression modulus B_p approaches zero, signaling the onset of instability. Fig 10 illustrates the relationship between B_p and biaxial stress P at three differ-

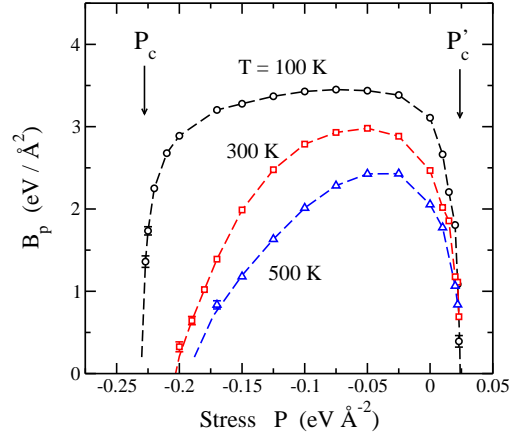


FIG. 10: Compression modulus B_p of silicene as a function of biaxial stress, derived from MD simulations for $T = 100$ K (circles), 300 K (squares), and 500 K (triangles). Lines are guides to the eye. P_c and P'_c indicate the spinodal pressure for tension (at $T = 100$ K) and compression, respectively.

ent temperatures: $T = 100$ K (circles), 300 K (squares), and 500 K (triangles). Under tensile stress, B_p exhibits qualitatively similar behavior across these temperatures. Starting from $P = 0$, the compression modulus initially increases with rising tension, reaching a maximum at a stress value that depends on the temperature, before decreasing as tension continues to increase. Eventually, B_p reaches zero at a critical pressure $P_c(T)$. Our simulations yield extrapolated values of $P_c = -0.23, -0.20$, and $-0.19 \text{ eV } \text{\AA}^{-2}$ for temperatures of $100, 300$, and 500 K, respectively, with an estimated error margin of $\pm 0.01 \text{ eV } \text{\AA}^{-2}$.

For compressive stress, we find $\partial B_p / \partial P < 0$ in all cases, with B_p vanishing at a critical pressure $P'_c = 24(1) \text{ meV } \text{\AA}^{-2}$, regardless of temperature, at least within the sensitivity limits of our current data for $P > 0$. These findings offer direct insight into the stability range of buckled silicene, which extends from a tensile critical pressure P_c to a compressive one P'_c . These pressures define the stability limits of silicene. Thus, for compressive pressure $P > P'_c$, the material adopts a corrugated phase, similar to that found earlier for graphene [25, 50]. Under tensions larger than P_c , atomic bonds break and one finds rupture of the material into small clusters.

It is noteworthy that the pressure dependence of B_p depicted in Fig. 10 is similar to the behavior observed for ice Ih under hydrostatic pressure [84]. This is an example where a 3D solid experiences mechanical instability for both compressive ($P > 0$) and tensile pressure ($P < 0$) within a relatively narrow pressure range, approximately 1 GPa for ice Ih.

For 2D solids, the functional dependence of the compression modulus on biaxial stress and in-plane area near a spinodal instability can be derived through series expansions of the pertinent thermodynamic variables.

Specifically, the Helmholtz free energy at temperature T can be expressed as a function of the area A_p as follows [85–87]:

$$F = F_c + r_1 (A_p - A_p^c) + r_3 (A_p - A_p^c)^3 + \dots \quad (4)$$

In this expression, F_c and A_p^c represent the free energy and in-plane area of the 2D system at the spinodal point, respectively. This formulation holds for $A_p > A_p^c$, meaning the approach to A_p^c occurs from above as A_p decreases ($P > 0$). The absence of a quadratic term on the right-hand side of Eq. (4) ($r_2 = 0$) ensures that the second derivative $\partial^2 F / \partial A_p^2$ vanishes at A_p^c , defining the thermodynamic stability limit for the system. Generally, the coefficients r_i are temperature-dependent.

The 2D compression modulus, $B_p = A_p \partial^2 F / \partial A_p^2$, can be approximated near the spinodal point by:

$$B_p = 6r_3 A_p^c (A_p - A_p^c). \quad (5)$$

Given that $P = -\partial F / \partial A_p$, we obtain:

$$P = P'_c - 3r_3 (A_p - A_p^c)^2 + \dots, \quad (6)$$

where $P'_c = -r_1$ represents the spinodal pressure corresponding to the area A_p^c . From Eqs. (5) and (6), we can derive:

$$B_p = 2A_p^c \sqrt{3r_3(P'_c - P)}. \quad (7)$$

As noted earlier, these expressions are applicable when the system approaches a spinodal point from $A_p > A_p^c$ or $P < P'_c$. When approaching a spinodal point from the opposite direction, i.e., for $P > P_c$ (increasing tension, $P < 0$ in this context), the terms should be adjusted as follows: replace $(A_p - A_p^c)$ with $(A_p^c - A_p)$ in Eqs. (4), (5), and (6), and substitute $P - P_c$ in Eq. (7), where $P_c = r_1$.

According to Eq. (7), B_p vanishes at both P'_c and P_c , accompanied by a singularity in $\partial B_p / \partial P$, indicating a divergence in compressibility. For the in-plane area near the compressive stress P'_c , we have $A_p - A_p^c \sim \sqrt{P_c - P}$, aligning with the trend shown in Fig. 5 for $P > 0$. For tensile pressure near P_c , a similar behavior of A_p is expected, with a divergence in the derivative $\partial A_p / \partial P$. However, this singularity is less apparent in Fig. 5, as the silicene structure tends to become unstable in MD simulations before reaching P_c , particularly at higher temperatures where larger area fluctuations occur.

It is worthwhile to discuss the influence of system size on the spinodal pressures calculated for silicene. For tensile stress, no significant dependence on the system size N is observed for the value of P_c . However, the situation differs for compressive stress P'_c , which tends to decrease as the system size N increases. Our MD simulation results show that P'_c takes values of 42, 24, and 13 meV \AA^{-2} for system sizes $N = 60, 112$, and 216, respectively. This indicates a trend where P'_c approaches zero as N becomes larger.

For a simulation cell of size N (with an area NA_p), the effective wavelength cutoff λ_{\max} is approximately equal

to the side length of the cell, $L = (NA_p)^{1/2}$. This corresponds to a minimum wavenumber $k_{\min} = 2\pi/\lambda_{\max}$, implying $k_{\min} \sim N^{-1/2}$. To relate this to the size dependence of P_c , we note that the frequency of the out-of-plane ZA modes for silicene under biaxial stress P is described by $\rho\omega^2 = \gamma k^2 + \kappa k^4$, where $\gamma = \gamma_0 - P$ [25, 88]. As compressive stress ($P > 0$) increases, γ decreases, leading to $d\omega/dP < 0$. This indicates that for a system of size N , the silicene sheet becomes unstable when the frequency of the ZA mode at k_{\min} approaches zero. This condition is met when $\gamma_c = -\kappa k_{\min}^2$.

Assuming that the residual intrinsic stress, γ_0 , can be considered negligible for our analysis, we have $P'_c = -\gamma_c$. The spinodal pressure is therefore given by:

$$P'_c = \kappa k_{\min}^2 = \frac{4\pi^2\kappa}{NA_p}. \quad (8)$$

Substituting into this expression the values $\kappa = 0.39$ eV and $A_p = 6.326$ $\text{\AA}^2/\text{atom}$, we find at $T = 300$ K the following results: $P'_c = 41, 22$, and 11 meV \AA^{-2} for $N = 60, 112$, and 216, respectively. These calculated values are slightly lower than those obtained from our simulations. Specifically, for the system size examined in detail in this study, $N = 112$, Eq. (8) predicts $P'_c = 22$ meV \AA^{-2} , which can be compared to a critical pressure of 24 meV \AA^{-2} determined from our simulations by identifying the point where the modulus B_p approaches zero (see Fig. 10).

Discrepancies between both sets of data for P'_c may be attributed to the presence of a residual intrinsic stress γ_0 at $T = 300$ K [25]. Additionally, fluctuations in the in-plane area A_p during our simulations near the spinodal pressure can lead to an early indication of the actual transition (spinodal) point. This effect is particularly pronounced in smaller system sizes, where the relative fluctuation $\Delta A_p / A_p$ is more significant. Further checking of this behavior would require extended simulations with larger system sizes than those currently considered. However, such simulations are presently infeasible due to the substantial computational resources required by the TB Hamiltonian utilized in this study. In this context, we note that similar MD simulations of graphene bilayers, performed with an empirical interatomic potential, have demonstrated a dependency of $B_p \sim 1/N$ at room temperature for systems containing up to thousands of atoms per layer [88].

The instability at tensile stress P'_c arises from the weakening of Si–Si bonds for large interatomic distances, and is not associated with the divergence of out-of-plane fluctuations linked to the vanishing frequencies in the ZA phonon branch. Consequently, this type of instability does not exhibit a similar size effect as that found for compressive pressure P_c . However, the actual value of P'_c is temperature-dependent, as higher temperatures increase the MSD of Si atoms, thereby promoting bond weakening.

IV. SUMMARY

Molecular dynamics simulations offer a powerful and reliable method for investigating the elastic properties of 2D materials and assessing their mechanical stability under diverse stress conditions. In this study, we presented and analyzed simulation results for silicene, employing a dependable TB Hamiltonian across a wide range of in-plane stresses and temperatures. Our analysis centered on key properties, including Si-Si bond length, in-plane area, atomic mean-square displacements, elastic constants, and 2D compression modulus.

For the stress-free material at low temperatures, the in-plane area A_p decreases as T rises, reaching a minimum at approximately $T = 450$ K, before increasing at higher temperatures. Under tensile stress, the low- T negative thermal expansion of A_p vanishes due to a reduction in out-of-plane vibrational amplitudes.

Our results indicate that the elastic stiffness constants c_{11} and c_{12} , as well as the compression modulus and Poisson's ratio of silicene, show a significant decrease with increasing temperature. The modulus B_p , a key thermodynamic variable in our analysis, was determined using three different methods: (1) from the elastic constants, (2) from in-plane area fluctuations, and (3) through numerical derivation of the $P - A_p$ equation of state. The agreement among the results from all three approaches confirms the consistency of our calculations.

At a given temperature, we observed instabilities in the silicene structure under specific tensile and compressive biaxial stresses, denoted as P_c and P'_c , which mark the boundaries of the material's mechanical stability or spinodal points. As these critical pressure values are approached, various properties exhibit anomalies, with some showing clear divergences. Notably, pronounced divergences were detected in the atomic MSDs, $(\Delta z)^2$ and $(\Delta \mathbf{r}_p)^2$, as well as in the in-plane area A_p .

A clear indication of the mechanical instability limits is given by the vanishing of the modulus B_p , which corresponds to a divergence in compressibility at the spinodal points. The tensile pressure P_c is temperature-dependent, varying from -0.23 to -0.19 eV Å⁻² over the temperature range of 100 to 500 K. For the spinodal compressive pressure P'_c , our MD simulations do not reveal a significant temperature dependence; however, a system-size effect has been observed, indicating that P_c scales approximately as $1/N$.

MD simulations, like those presented here, can also provide valuable insights into the behavior of silicene multilayers under stress, shedding light on the mechanical stability of these 2D materials under tensile and compressive conditions. Additionally, nuclear quantum effects may play a role in influencing the elastic properties of silicene and other crystalline membranes at low temperatures. This aspect can be explored through atomic-scale simulations using methods such as path-integral molecular dynamics. When combined with electronic structure techniques, these methods form a powerful approach for unraveling the complex dynamics of 2D materials.

Data availability

The data that support the findings of this study are available from the corresponding author upon reasonable request.

CRediT author contribution statement

Carlos P. Herrero: Data curation, Investigation, Validation, Original draft

Rafael Ramírez: Methodology, Software, Investigation, Validation

Declaration of Competing Interest

The authors declare that they have no known competing financial interests or personal relationships that could have appeared to influence the work reported in this paper.

Acknowledgments

Miguel del Canizo is thanked for his comments and discussions on molecular dynamics simulations of silicene. This work was supported by Ministerio de Ciencia e Innovación (Spain) under Grant Number PID2022-139776NB-C66.

-
- [1] H. J. W. Zandvliet, *Nano Today* **9**, 691 (2014).
 - [2] L. Tao, E. Cinquanta, D. Chiappe, C. Grazianetti, M. Fanciulli, M. Dubey, A. Molle, and D. Akinwande, *Nature Nanotech.* **10**, 227 (2015).
 - [3] C. Grazianetti, E. Cinquanta, and A. Molle, *2D Mater.* **3**, 012001 (2016).
 - [4] A. Molle, C. Grazianetti, L. Tao, D. Taneja, M. H. Alam, and D. Akinwande, *Chem. Soc. Rev.* **47**, 6370 (2018).
 - [5] M. A. Kharadi, G. F. A. Malik, F. A. Khanday, K. A. Shah, S. Mittal, and B. K. Kaushik, *ECS J. Solid State Sci. Techn.* **9**, 115031 (2020).
 - [6] C. Tantardini, A. G. Kvashnin, C. Gatti, B. Yakobson, I. and X. Gonze, *ACS Nano* **15**, 6861 (2021).
 - [7] S. Ghosal, A. Bandyopadhyay, S. Chowdhury, and D. Jana, *Rep. Progr. Phys.* **86**, 096502 (2023).
 - [8] Z. Ni, Q. Liu, K. Tang, J. Zheng, J. Zhou, R. Qin, Z. Gao,

- D. Yu, and J. Lu, *Nano Lett.* **12**, 113 (2012).
- [9] Z.-X. Guo, Y.-Y. Zhang, H. Xiang, X.-G. Gong, and A. Oshiyama, *Phys. Rev. B* **92**, 201413 (2015).
- [10] J. Zhu and U. Schwingenschlogl, *2D Mater.* **3**, 035012 (2016).
- [11] Q. Guo, J. Liu, C. Bai, N. Chen, and L. Qu, *ACS Nano* **15**, 16533 (2021).
- [12] H. H. Gurel and B. Salmankurt, *Biosensors* **11**, 59 (2021).
- [13] G. Guo, Y. Xu, and G. Guo, *J. Phys.: Condens. Matter* **35**, 335501 (2023).
- [14] G. Guo, J. Liu, Y. Xu, G. Guo, and S. Tan, *Colloids and Surfaces A* **667**, 131379 (2023).
- [15] T.-N. Do, G. Gumbs, P.-H. Shih, D. Huang, C.-W. Chiu, C.-Y. Chen, and M.-F. Lin, *Sci Rep.* **9**, 624 (2019).
- [16] S. A. Safran, *Statistical Thermodynamics of Surfaces, Interfaces, and Membranes* (Addison Wesley, New York, 1994).
- [17] D. Nelson, T. Piran, and S. Weinberg, *Statistical Mechanics of Membranes and Surfaces* (World Scientific, London, 2004).
- [18] D. Nelson and L. Peliti, *J. Phys.* **48**, 1085 (1987).
- [19] P. Le Doussal and L. Radzihovsky, *Phys. Rev. Lett.* **69**, 1209 (1992).
- [20] A. Kosmrlj and D. R. Nelson, *Phys. Rev. E* **88**, 012136 (2013).
- [21] A. Kosmrlj and D. R. Nelson, *Phys. Rev. E* **89**, 022126 (2014).
- [22] E. Chacón, P. Tarazona, and F. Bresme, *J. Chem. Phys.* **143**, 034706 (2015).
- [23] T. Ruiz-Herrero, E. Velasco, and M. F. Hagan, *J. Phys. Chem. B* **116**, 9595 (2012).
- [24] B. Amorim, R. Roldan, E. Cappelluti, A. Fasolino, F. Guinea, and M. I. Katsnelson, *Phys. Rev. B* **89**, 224307 (2014).
- [25] R. Ramírez and C. P. Herrero, *J. Chem. Phys.* **149**, 041102 (2018).
- [26] R. Ramírez, P. Tarazona, E. Chacón, and C. P. Herrero, *Phys. Rev. B* **108**, 165417 (2023).
- [27] B. Ipaves, J. F. Justo, and L. V. C. Assali, *Phys. Chem. Chem. Phys.* **24**, 8705 (2022).
- [28] B. Mortazavi, O. Rahaman, M. Makaremi, A. Dianat, G. Cuniberti, and T. Rabczuk, *Physica E* **87**, 228 (2017).
- [29] C. Qian and Z. Li, *Comp. Mater. Sci.* **172**, 109354 (2020).
- [30] S. Yoo, B. Lee, and K. Kang, *Nanotech.* **32**, 295702 (2021).
- [31] J. Zeng, M. Wu, B. Xu, S. Tao, X. Li, and C. Ouyang, *J. Mater. Sci.* **53**, 4306 (2018).
- [32] H. Zhao, *Phys. Lett. A* **376**, 3546 (2012).
- [33] R. Qin, C.-H. Wang, W. Zhu, and Y. Zhang, *AIP Adv.* **2**, 022159 (2012).
- [34] M. R. Chavez-Castillo, M. A. Rodriguez-Meza, and L. Meza-Montes, *RSC Adv.* **8**, 10785 (2018).
- [35] D. K. Das and J. Sarkar, *J. Appl. Phys.* **123**, 044304 (2018).
- [36] Y.-C. Fan, T.-H. Fang, and T.-H. Chen, *Nanomater.* **6**, 120 (2016).
- [37] M. Hu, X. Zhang, and D. Poulidakos, *Phys. Rev. B* **87**, 195417 (2013).
- [38] Q.-X. Pei, Z.-D. Sha, Y.-Y. Zhang, and Y.-W. Zhang, *J. Appl. Phys.* **115**, 023519 (2014).
- [39] S. Rouhi, H. Pourmirzaagha, and A. Farzin, *Mater. Res. Express* **6**, 085004 (2019).
- [40] G. R. Berdiyorov and F. M. Peeters, *RSC Adv.* **4**, 1133 (2014).
- [41] T. K. Min, T. L. Yoon, and T. L. Lim, *Mater. Res. Express* **5**, 065054 (2018).
- [42] Z. Wang, T. Feng, and X. Ruan, *J. Appl. Phys.* **117**, 084317 (2015).
- [43] A. Ince and S. Erkoç, *Comp. Mater. Sci.* **50**, 865 (2011).
- [44] N. T. Long, T. Q. Tuan, D. N. A. Thuy, Q. D. Ho, and H. A. Huy, *Molec. Simul.* **49**, 655 (2023).
- [45] C. Qian and J. Wang, *RSC Advances* **10**, 33129 (2020).
- [46] C. P. Herrero and M. del Canizo, *J. Phys. Chem. Solids* **196**, 112343 (2024).
- [47] S. Rouhi, *Comp. Mater. Sci.* **131**, 275 (2017).
- [48] J. Zhao, H. Liu, Z. Yu, R. Quhe, S. Zhou, Y. Wang, C. C. Liu, H. Zhong, N. Han, J. Lu, et al., *Prog. Mater. Sci.* **83**, 24 (2016).
- [49] L. Masson and G. Prevot, *Nanoscale Adv.* **5**, 1574 (2023).
- [50] R. Ramírez and C. P. Herrero, *Phys. Rev. B* **95**, 045423 (2017).
- [51] G. Panzarini and L. Colombo, *Phys. Rev. Lett.* **73**, 1636 (1994).
- [52] M. Kaczmarek, O. N. Bedoya-Martinez, and E. R. Hernandez, *Phys. Rev. Lett.* **94**, 095701 (2005).
- [53] R. Car and M. Parrinello, *Phys. Rev. Lett.* **55**, 2471 (1985).
- [54] C. P. Herrero and R. Ramírez, *J. Phys.: Condens. Matter* **26**, 233201 (2014).
- [55] C. P. Herrero and R. Ramírez, *J. Chem. Phys.* **145**, 224701 (2016).
- [56] C. P. Herrero and R. Ramírez, *J. Phys. Chem. Solids* **171**, 110980 (2022).
- [57] D. Porezag, T. Frauenheim, T. Köhler, G. Seifert, and R. Kaschner, *Phys. Rev. B* **51**, 12947 (1995).
- [58] T. Frauenheim, F. Weich, T. Kohler, S. Uhlmann, D. Porezag, and G. Seifert, *Phys. Rev. B* **52**, 11492 (1995).
- [59] C. M. Goringe, D. R. Bowler, and E. Hernández, *Rep. Prog. Phys.* **60**, 1447 (1997).
- [60] P. Klein, H. M. Urbassek, and T. Frauenheim, *Comp. Mater. Sci.* **13**, 252 (1999).
- [61] P. Klein, H. M. Urbassek, and T. Frauenheim, *Phys. Rev. B* **60**, 5478 (1999).
- [62] S. A. Shevlin, A. J. Fisher, and E. Hernandez, *Phys. Rev. B* **63**, 195306 (2001).
- [63] R. Gutierrez, T. Frauenheim, T. Köhler, and G. Seifert, *J. Mater. Chem.* **6**, 1657 (1996).
- [64] R. Ramírez, C. P. Herrero, E. R. Hernández, and M. Cardona, *Phys. Rev. B* **77**, 045210 (2008).
- [65] C. P. Herrero, R. Ramírez, and G. Herrero-Saboya, *Phys. Rev. B* **109**, 104112 (2024).
- [66] R. Ramírez and C. P. Herrero, *Phys. Rev. B* **101**, 235436 (2020).
- [67] R. Rurali and E. Hernandez, *Comp. Mater. Sci.* **28**, 85 (2003).
- [68] J.-B. Fournier and C. Barbetta, *Phys. Rev. Lett.* **100**, 078103 (2008).
- [69] H. Shiba, H. Noguchi, and J.-B. Fournier, *Soft Matter* **12**, 2373 (2016).
- [70] M. E. Tuckerman and A. Hughes, in *Classical and Quantum Dynamics in Condensed Phase Simulations*, edited by B. J. Berne, G. Ciccotti, and D. F. Coker (World Scientific, Singapore, 1998), p. 311.
- [71] M. P. Allen and D. J. Tildesley, *Computer simulation of liquids* (Clarendon Press, Oxford, 1987).
- [72] G. J. Martyna, M. E. Tuckerman, D. J. Tobias, and M. L. Klein, *Mol. Phys.* **87**, 1117 (1996).

- [73] S. Cahangirov, M. Topsakal, E. Akturk, H. Sahin, and S. Ciraci, Phys. Rev. Lett. **102**, 236804 (2009).
- [74] H. Sahin, S. Cahangirov, M. Topsakal, E. Bekaroglu, E. Akturk, R. T. Senger, and S. Ciraci, Phys. Rev. B **80**, 155453 (2009).
- [75] E. Scalise, M. Houssa, G. Pourtois, B. van den Broek, V. Afanas'ev, and A. Stesmans, Nano Res. **6**, 19 (2013).
- [76] T. Jaroch, M. Krawiec, and R. Zdyb, 2D Mater. **8**, 035038 (2021).
- [77] F. Behroozi, Langmuir **12**, 2289 (1996).
- [78] J. C. Garcia, D. B. de Lima, L. V. C. Assali, and J. F. Justo, J. Phys. Chem. C **115**, 13242 (2011).
- [79] N. W. Ashcroft and N. D. Mermin, *Solid State Physics* (Saunders College, Philadelphia, 1976).
- [80] B. Marsden, A. Mummery, and P. Mummery, Proc. Royal Soc. A **474**, 20180075 (2018).
- [81] R. Qin, W. Zhu, Y. Zhang, and X. Deng, Nanoscale Research Lett. **9**, 521 (2014).
- [82] C. P. Herrero and R. Ramírez, J. Chem. Phys. **148**, 102302 (2018).
- [83] L. D. Landau and E. M. Lifshitz, *Statistical Physics* (Pergamon, Oxford, 1980), 3rd ed.
- [84] C. P. Herrero and R. Ramírez, Phys. Rev. B **84**, 224112 (2011).
- [85] R. J. Speedy, J. Phys. Chem. **86**, 3002 (1982).
- [86] H. J. Maris, Phys. Rev. Lett. **66**, 45 (1991).
- [87] J. Boronat, J. Casulleras, and J. Navarro, Phys. Rev. B **50**, 3427 (1994).
- [88] C. P. Herrero and R. Ramírez, Eur. Phys. J. B **96**, 147 (2023).